Supporting Information for

Probing Electric Double Layer Composition via in-situ Vibrational Spectroscopy and Molecular Simulations

Jonathan H. Raberg[1+], Jenel Vatamanu,[2] Stephen J. Harris[3], Christina H. M. van Oversteeg[4], Axel Ramos[1], Oleg Borodin,[2] and Tanja Cuk[1,5,] †*

[1] Department of Chemistry, University of California, Berkeley, Berkeley, CA 94720 United States

[2] Electrochemistry Branch, Sensor and Electron Devices Directorate, Power and Energy Division, U.S. Army Research Laboratory, Adelphi, MD 20783, United States

[3] Materials Science Division, Lawrence Berkeley National Lab, Berkeley, CA 94720, United States

[4] Debye Institute for Nanomaterials Science, Utrecht University, 3508 TA Utrecht, The Netherlands

[5] Chemical Science Division, Lawrence Berkeley National Lab, Berkeley, CA 94720, United States

Density Functional Study of Solvated IR Spectra

A DMC molecule is conformationally flexible adopting two main conformers cis-cis (cc) and cis-trans (ct) as shown in Figure S1. In gas phase the DMC(cc) conformer is more energetically favorable than DMC(ct) by ~3 kcal/mol, resulting in the dominance of DMC(cc) conformer in gas-phase and pure liquid.[1-3] Previous Raman measurements also estimated DMC(ct) population is only 6% of DMC(cc).[3] Thus, we compare DMC(cc) vibrational bands from DFT calculations with IR experiments in Table S1 and DMC(cc) is the predominant conformer. In agreement with the previous work,[3] we assigned vibrational bands around 1278 cm^{-1} and 1754 cm^{-1} to OCO asymmetric bend and C=O stretch modes for DMC(cc) conformer. Two DFT functionals: PBE and B3LYP were used in calculations in conjunction with two basis sets: a smaller 6-31+G(d,p) and a larger aug-cc-pvTz (denoted as Tz). All complexes were immersed in implicit solvent with a dielectric constant ε=3.0473 modeled using a solvation model based on electron density (SMD) in order to mimic DMC behavior in a liquid phase.[4] PBE/6-31+G(d,p) and B3LYP/aug-cc-pvTz calculations predicted frequencies in close agreement to experimental observations. DFT calculations indicate that DMC(ct) vibrational modes are slightly shifted compared to DMC(cc). Specifically, ν_{OCO}(asym) band is consistently red shifted by 8-22 cm^{-1}, while $\nu_{C=O}$ symmetric stretch is blue shifted by 15-17 cm^{-1}. The differences between DMC(cc) and DMC(ct) band positions are smaller than the width of the experimentally observed peaks shown in Figure 1b, thus small fraction of DMC(ct) only contributes to a slight asymmetry of the observed peaks and cannot be easily observed in IR.

Next, we examine the influence of a Li^+ cation on vibrational modes using a simplified DMC/Li^+ solvate before examination of a more realistic DMC_3-$LiClO_4$ solvate. DFT calculations for the DMC(cc)/Li^+

complexes with Li^+ bound to a carbonyl oxygen indicate that ν_{OCO}(asym) band is blue shifted by 65-76 cm^{-1}, while $\nu_{C=O}$ band is red shifted by 59-74 cm^{-1}. Similar shifts in magnitude and direction were observed for the DMC(ct) bands upon Li^+ complexation. Li^+ binding to non-carbonyl oxygens, however, resulted in shifting ν_{OCO}(asym) and $\nu_{C=O}$ bands in the opposite direction compared to DMC/Li^+ with Li^+ binding to carbonyl oxygen. PBE/6-31+G(d,p) yields similar magnitudes of shifts to those found in DFT calculations using a much larger and more computationally expensive aug-cc-pvTz basis set. Thus, we adopted PBE/6-31+G(d,p) for investigation of the much larger DMC$(cc)_3$-$LiClO_4$ and DMC$(cc)_2$DMC(ct)-$LiClO_4$-solvates that explicitly and more realistically represent the Li^+ first solvation shell. DFT calculations on these solvates yielded smaller shift factors of 35/37 cm^{-1} for ν_{OCO}(asym) and -32/-31 cm^{-1} for $\nu_{C=O}$ stretch as shown in Table 1 and Figure S1. These numbers are in good agreement with the shifts obtained from fits to experimental data further confirming band assignment to the free and complexed DMC molecules and indicating that Li^+ preferentially binds to carbonyl oxygen atoms.

DFT calculations also predicted that intensity of the DMC/Li^+ ν_{OCO} (asym) bend is reduced to 0.75-0.76 of pure DMC(cc), while intensity of the DMC $\nu_{C=O}$ band increases by factor of 1.37 upon Li^+ complexation.

Presence of the Li^+ near ClO_4^- band resulted in the split into three peaks, two of which have close positions as shown in Figure S2.

	PBE/ 6-31+G(d,p)	PBE/Tz[a]	B3LYP/ 6-31+G(d,p)	B3LYP/Tz[a]	exp
			DMC(cc)		
ν_{OCO} (asym)	1265	1241	1317	1292	1278
$\nu_{C=O}$	1740	1727	1782	1771	1754
	scaling factor for DMC(cc) vs. experiment for pure DMC liquid				
ν_{OCO} (asym)	0.990	0.971	1.031	1.011	
$\nu_{C=O}$	0.992	0.985	1.016	1.010	
			DMC(ct)		
ν_{OCO} (asym)	1243	1233	1296	1282	
$\nu_{C=O}$	1755	1741	1799	1786	
			DMC(cc)/Li^+		
ν_{OCO} (asym)	1333	1317	1382	1367	
$\nu_{C=O}$	1682	1664	1716	1697	
			DMC(ct)/Li^+		
ν_{OCO} (asym)	1324	1311	1371	1358	
$\nu_{C=O}$	1683	1663	1719	1699	
	DMC(cc, EO)/Li^+ (Li is bound no non-carbonyl oxygens)				
ν_{OCO} (asym)	1182	1155	1231	1206	
$\nu_{C=O}$	1822	1813	1869	1859	
			DMC(cc)/Li^+ shifts vs. DMC(cc)		
ν_{OCO} (asym)	68	76	65	75	
$\nu_{C=O}$	-59	-64	-67	-74	
			DMC(ct)/Li^+ shifts vs. DMC(cc)		
ν_{OCO} (asym)	59	70	54	66	
$\nu_{C=O}$	-57	-64	-64	-72	
			DMC(cc)/Li^+ intensity ratios vs. DMC(cc)		
ν_{OCO} (asym)	0.78	0.83	0.82	0.87	
$\nu_{C=O}$	1.45	1.29	1.39	1.41	
			DMC(cc)/Li^+ intensity ratios vs. DMC(cc)		

Table S1. DFT calculation results for frequencies (in cm^{-1}) of the DMC and DMC/Li+ complexes immersed in polarized continuum using SMD(ε=3.0473) solvation model and the associated frequency shifts and IR intensity ratios due to DMC complexation to the Li^+ cation.

ν_{OCO} (asym)	0.62	0.65	0.65	0.58
$\nu_{C=O}$	1.90	1.99	1.84	1.75

[a] Tz denotes aug-cc-pvTz basis set

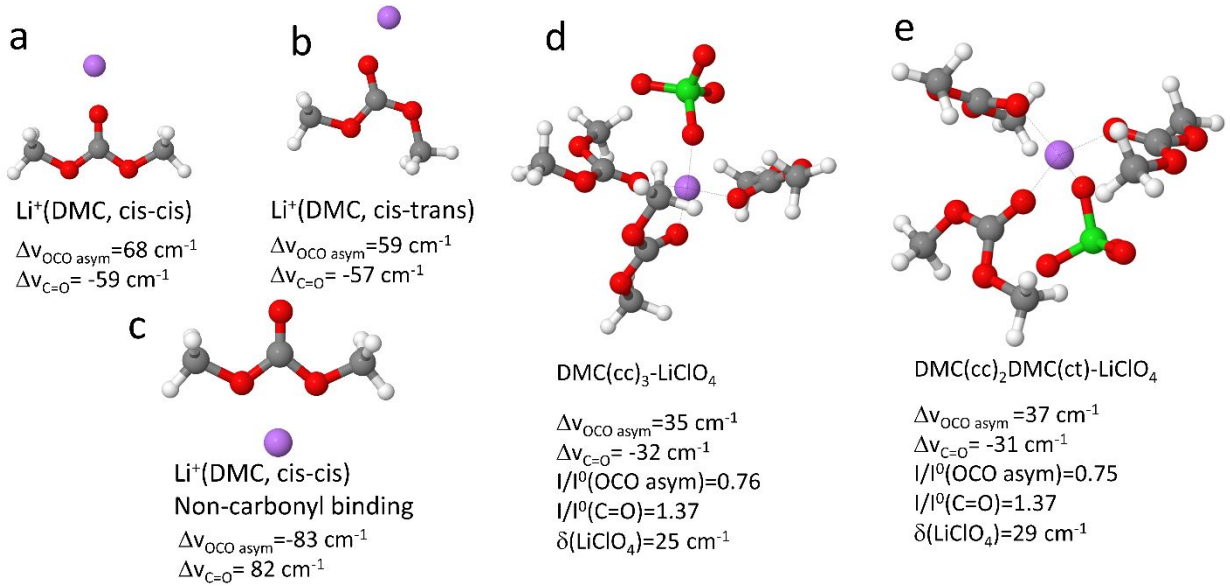

Figure S1. Optimized geometries of the DMC/Li^+ and $DMC_3(LiClO_4)$ clusters from PBE/6-31+G(d,p) calculations using SMD(ε=3.0473) implicit solvent model and the associated shifts in frequencies (Δv) and IR intensity ratios (I/I_0) vs. DMC(cc). $\delta(LiClO_4)$ denote the difference between the blue and red shifted ClO_4^- peaks upon the Li^+ cation complexation.

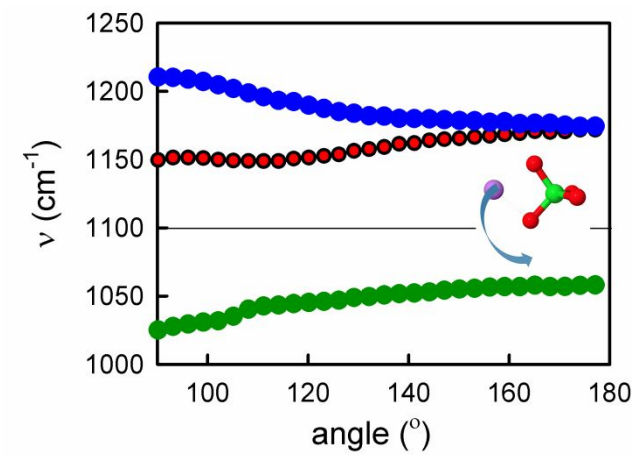

Figure S2. Dependence of the ClO4- anion vibrational band on the Li…O-Cl bending angle from M05-2X/aug-cc-pvTz calculations using SMD(e=3.0473) implicit solvent model.

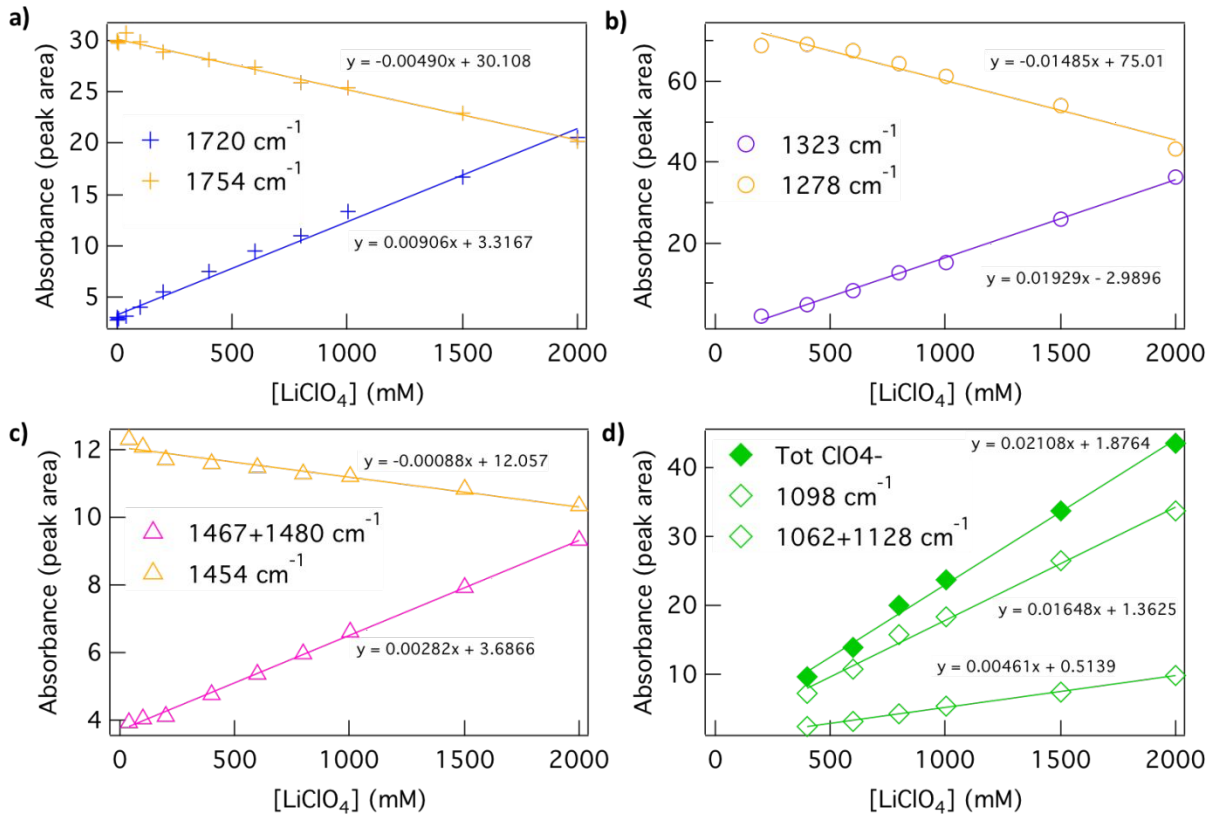

Figure S3. Concentration calibration with linear fits. Li^+---DMC peaks (blue, purple, pink) are shown with their Free-DMC counterparts (orange) in (a-c). All ClO_4^- peaks are shown in (d), with the total ClO_4^- used in analysis along with the free ClO_4^- (1098 cm^{-1}) and CIP ClO_4^- (1062 + 1128 cm^{-1}) alone.

Experimental Extraction of Molar Extinction Coefficient

The molar extinction coefficient, ε, can be determined from the calibration in Figure S3 using Beer's Law

$$A = \varepsilon c l$$

In an ATR geometry, the path length is defined as being equal to the product of the effective penetration depth (d_{eff}) and the number of internal bounces within the crystal ($N_{bounces}$),

$$l = d_{eff} N_{bounces}$$

The effective penetration depth is given by

$$d_{eff} = \frac{\lambda}{2\pi n_c \sqrt{sin^2\theta - (n_s/n_c)^2}}$$

where λ and θ are the wavelength and angle of incident light and n_c and n_s are the refractive indices of the crystal and sample, respectively. Beer's Law then becomes,

$$A = \varepsilon c d_{eff} N_{bounces}$$

A plot of absorbance versus concentration (Figure 1_Supp) has slope,

$$m = \varepsilon d_{eff,Ge} N_{bounces,\,Ge}$$

where the subscript "Ge" has been added to indicate that the calibration was performed using a germanium crystal. The molar extinction coefficient is thus calculated from

$$\varepsilon = \frac{m}{d_{eff,\,Ge} N_{bounces,Ge}}$$

for each of the peaks in question. For the Germanium crystal, $N_{bounces,Ge} = 13$, while for the ZnSe on which Au was deposited for the voltage dependent measurements, $N_{bounces,\,ZnSe} = 8$.

Surface Characterization

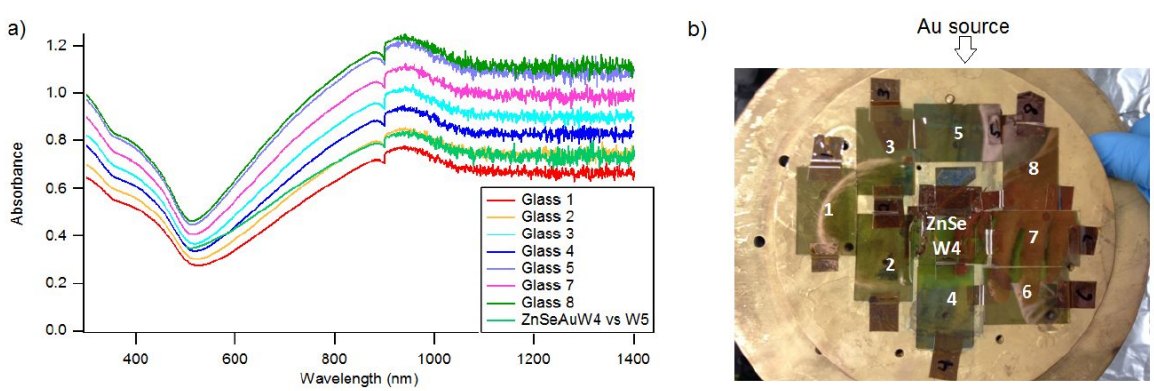

Figure S4. Thicknesses of the evaporated Au thin films were determined using UV-Vis transmittance at a wavelength of 1000 nm, using a calibration from Siegel et. al. (2012; http://dx.doi.org/10.5772/51617). It

was found that the thickness determined by UV-Vis was consistently about double the nominal evaporated thickness. Thicknesses were consistent to within ± 1 nm between evaporations.

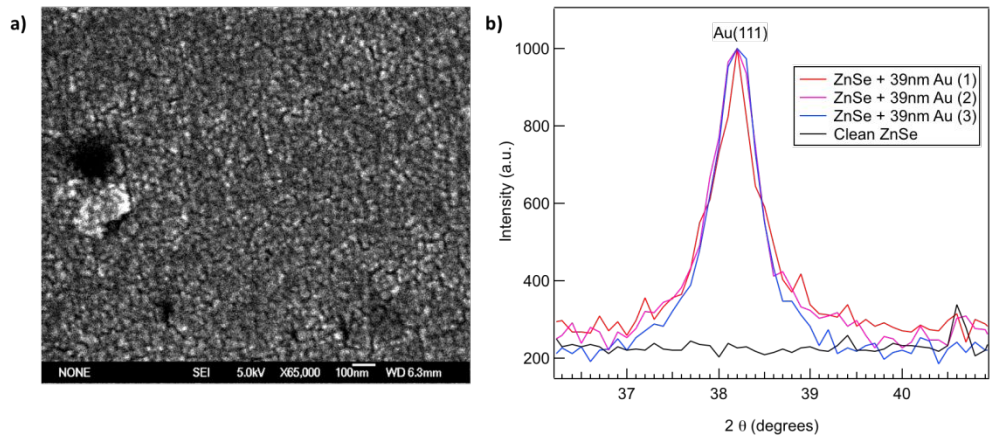

Figure S5: Surface structure of the Au thin films was further analyzed using SEM & XRD. The representative SEM image shown in a) reveals a relatively uniform nanoparticle-like gold surface with roughness on the order of 10-20 nm. XRD results in b) show Au(111) crystallites with a diameter ≤ 14 ± 1 nm as determined by the Scherrer equation (Dutta et. al., 1997; doi: 10.1016/S0040-6090(97)00220-4). No other Au crystal structures were observed.

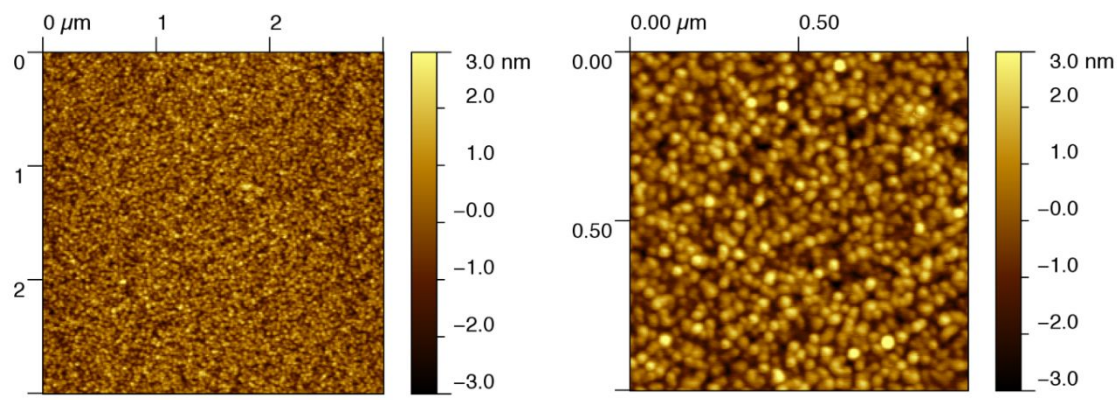

Figure S6: Roughness of ~ 10 nm was independently corroborated with AFM, with the above images. Courtesy of Chenghao Wu.

Voltage Dependent FTIR Spectra: Experimental Procedure

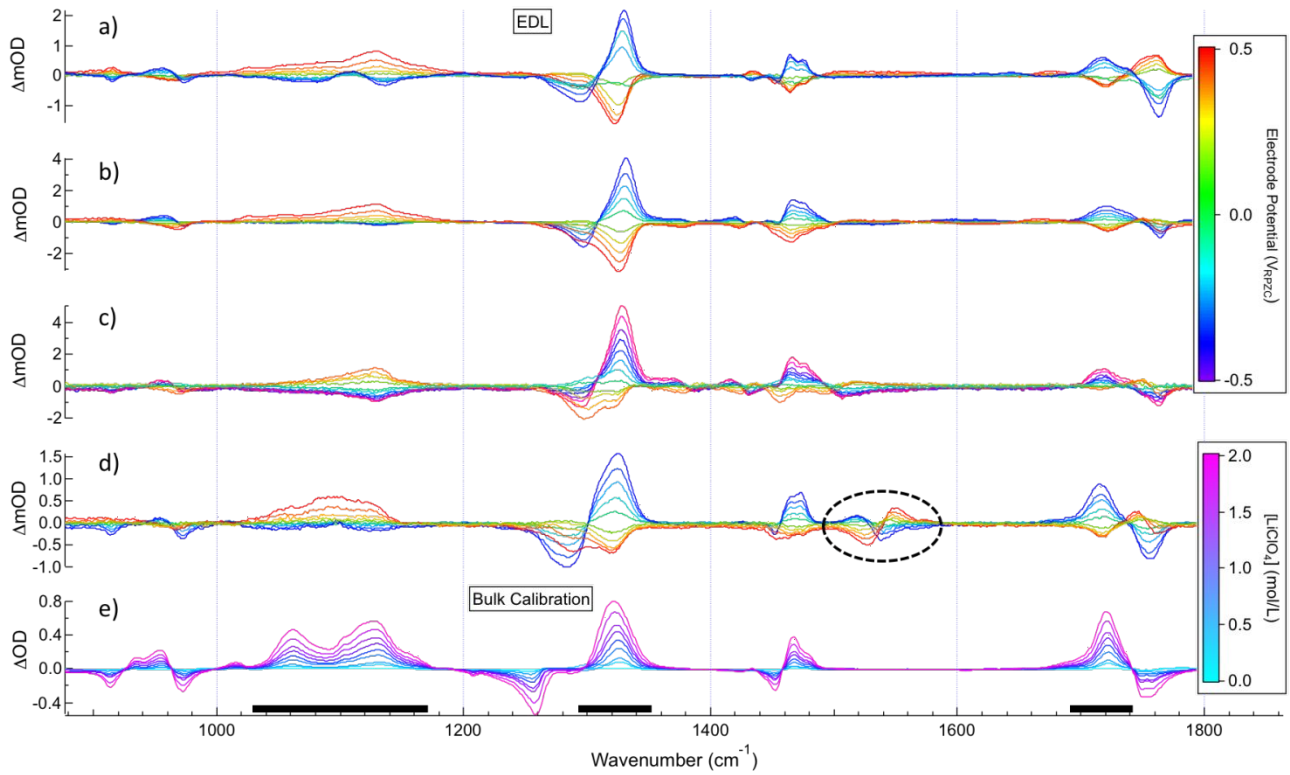

Figure S7: All voltage-dependent EDL trials (a-d) and the concentration-dependent bulk calibration (e). Regions fit for analysis are demarcated with black bars on the x-axis. Dashed circle in d) denotes an adsorbed species exhibiting a Stark effect.

The procedure for a given trial is as follows. First, the spectroelectrochemical cell is assembled and filled with 0.8 M $LiClO_4$/DMC in an N_2 glove box. The immersion potential is immediately measured as the open circuit (OC) voltage with respect to an Ag/$AgClO_4$ reference electrode. This voltage is taken to be a good approximation of the potential of zero charge (PZC) and is used as the reference potential for the rest of the experiment. A diagnostic current-voltage (CV) scan is performed with a range of ± 0.5 V_{RPZC}. The cell is subsequently moved from the glove box to a custom-built stand in a Bruker v70 FTIR and continuously purged with N_2.

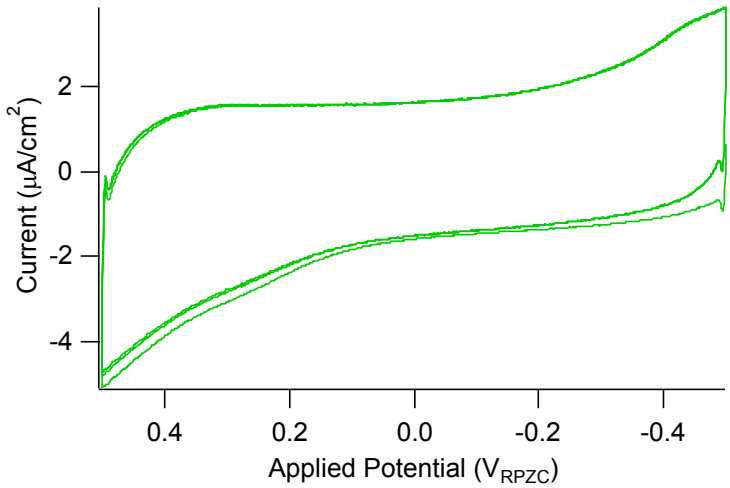

Figure S8. Representative CV of 0.8M $LiClO_4$/DMC in the spectroelectrochemical cell. The CV's are taken with a sweep rate of 0.1 V/s, such that they correspond to a capacitance of 20-40 uF/cm^2 between 0 V and +- 0.4 V.

To obtain EDL spectra at a given applied voltage, both a sample and reference spectrum must be taken. The reference spectrum is taken when the working electrode (WE) is held at the potential of zero charge. The sample spectrum is taken when the WE is held at the desired potential. To avoid problems of instrument drift, the WE is cycled between these two voltages. The resulting procedure is as follows (Figure 2.4_Supp): (1) The reference potential is applied and the EDL is allowed to charge (164 seconds). (2) A reference FTIR spectrum is taken (109 s). (3) The sample potential is applied and the EDL is allowed to charge (64 s). (4) A sample FTIR spectrum is taken (109 s). (5) The change in absorbance, ΔA, between the sample and reference spectra is calculated. (6) Steps 1-5 are performed repeatedly; the ΔA spectra generated in step 5 are averaged together until the desired signal-to-noise levels are reached (usually 4 cycles of 128 scans each). A non-capacitive current higher than 1 μA/cm^2 was never observed.

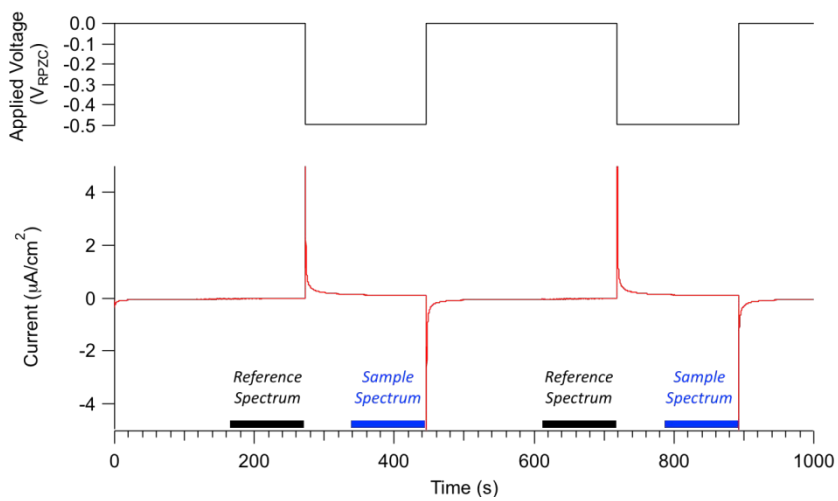

Applied voltage (top) and resulting current (bottom) for a typical trial. Time periods where reference and sample spectra are being taken are denoted with black and blue bars on the x-axis, respectively. Note that scale in the bottom plot is abbreviated; the maxima of the current spikes are ~3mA/cm^2.

Voltage-Dependent FTIR Spectra: Fitting details

Fits were performed using the Multi-peak Fit package in Igor Pro (v6.3). Gaussian fitting functions analogous to those from the bulk calibration were initialized by eye and optimized without constraints. Residuals were generally < 0.1 mOD. Optimized Li^+---DMC peak locations were within ± 5 cm^{-1} of the bulk calibration values. The broad ClO_4^- region produced higher variability, with locations up to 40 cm^{-1} from those found in the bulk in order to obtain the best overall fits. It must be noted that these discrepancies are due to the difference in shape between the EDL and bulk ClO_4^- absorptions. While this difference may be indicative of EDL-specific CIP or aggregate geometries, the overall strength of the ClO_4^- absorber is not expected to change.

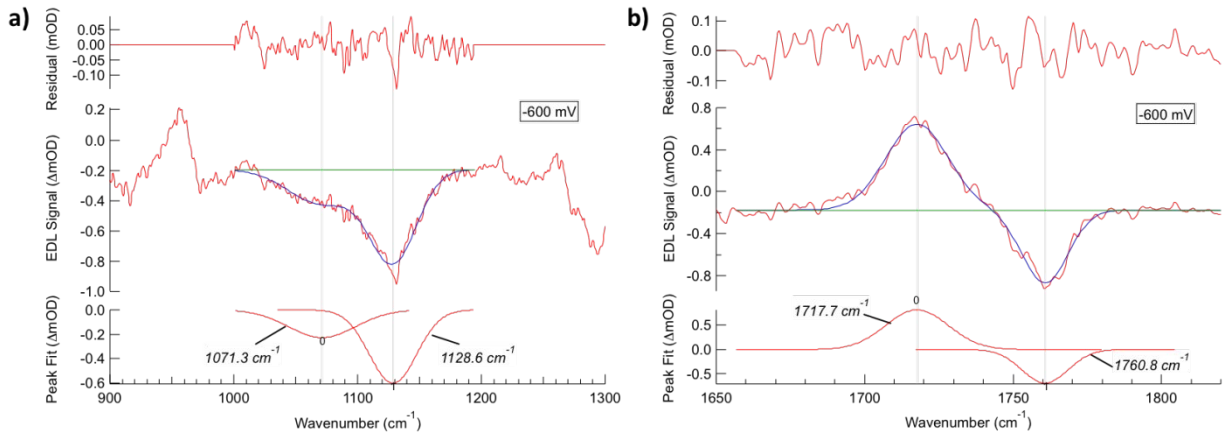

Representative fits for a) ClO_4^- and b) Li^+---DMC (-600mV, trial (c) in Figure S7).

To convert the voltage-dependent changes in peak area, ΔA, into a change in EDL ion number over a nm^2 of electrode, $\Delta n(\varphi)/nm^2$, the following derivation was used. In the EDL, changes in absorption are observed above a ZnSe crystal, resulting in the form of Beer's law,

$$\Delta A = \varepsilon \Delta c d_{eff,\,ZnSe} N_{bounces,\ ZnSe}$$

Substituting in the molar extinction coefficient, ε, from the earlier derivation,

$$\Delta A = \left(\frac{m}{d_{eff,Ge} N_{bounces,Ge}}\right) \Delta c d_{eff,\,ZnSe} N_{bounces,ZnSe}$$

The equation can be rearranged to yield,

$$\Delta c d_{eff,\,ZnSe} = \frac{\Delta A d_{eff,Ge}}{m} \cdot \frac{N_{bounces,Ge}}{N_{bounces,ZnSe}}$$

where $N_{bounces,Ge} = 13$, $N_{bounces,\,ZnSe} = 8$, and d_{eff} is a function of wavelength. The effective path length, $d_{eff,\,ZnSe}$, is never explicitly plugged in. Instead, we use the quantity $\Delta c d_{eff,\,ZnSe}$, which has units of ions/nm^2 and can be interpreted as a change in ion number over an area of electrode. The absorption equation then becomes $\boxed{\frac{\Delta n(\varphi)}{nm^2} = \Delta c d_{eff,\,ZnSe} = \frac{13}{8} \cdot \frac{\Delta A d_{eff,Ge}}{m}}$

This equation allows us to convert the observed voltage-dependent change in peak area, ΔA, into a change in EDL ion number over a nm^2 of electrode, $\Delta n(\varphi)/nm^2$.

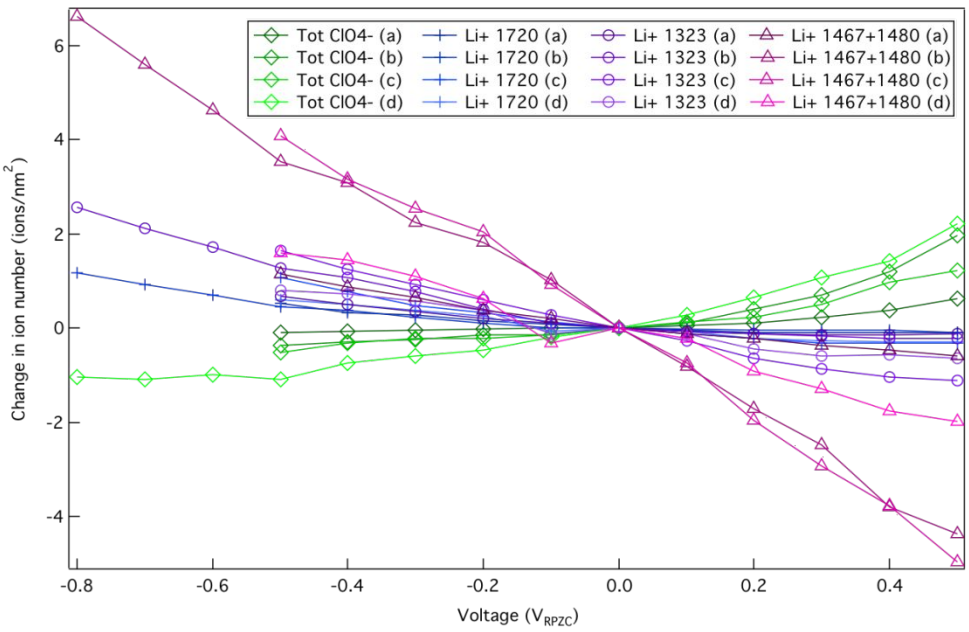

Figure S9: Calculated $\Delta n(\varphi)/nm^2$ for all peaks and all trials. The calculated $\Delta n(\varphi)/nm^2$ for all peaks and all trials is shown. Note that the voltage-dependent Li^+---DMC peaks at 1467+1480 cm^{-1} do not yield the same results for all four trials, with two of the trials out of the range of the other two Li^+---DMC peaks. This is likely due to overlapping features due to adsorbed species in the nearby frequency region which are trial dependent (e.g. trial d compared to trial c) and interfere with the peak fitting. Those data are shown here but were not included in the final analysis.

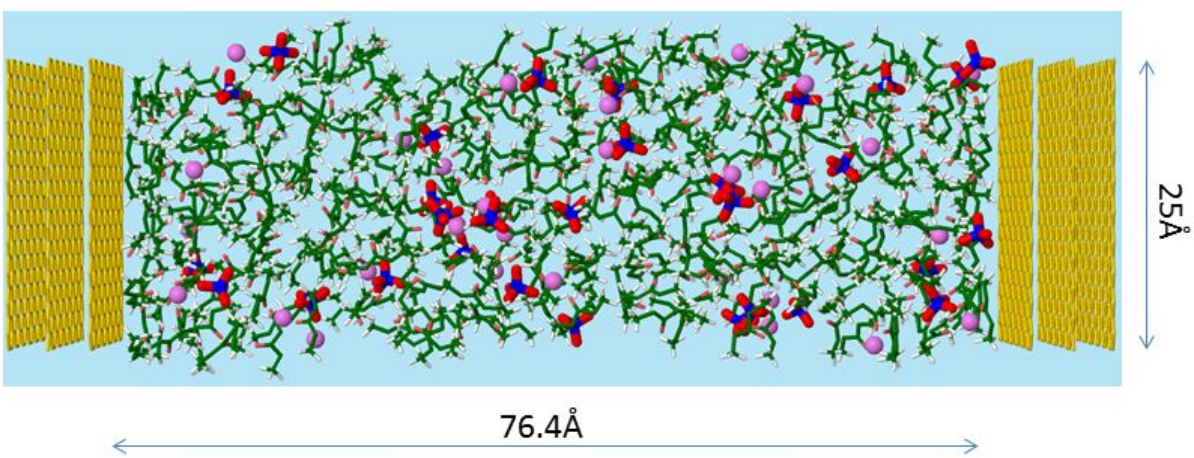

Figure S10. A snapshot of the MD setup utilized for the molecular simulations of electrode-electrolyte system. The numbers in the Figure show the typical system sizes utilized in Angstrom.

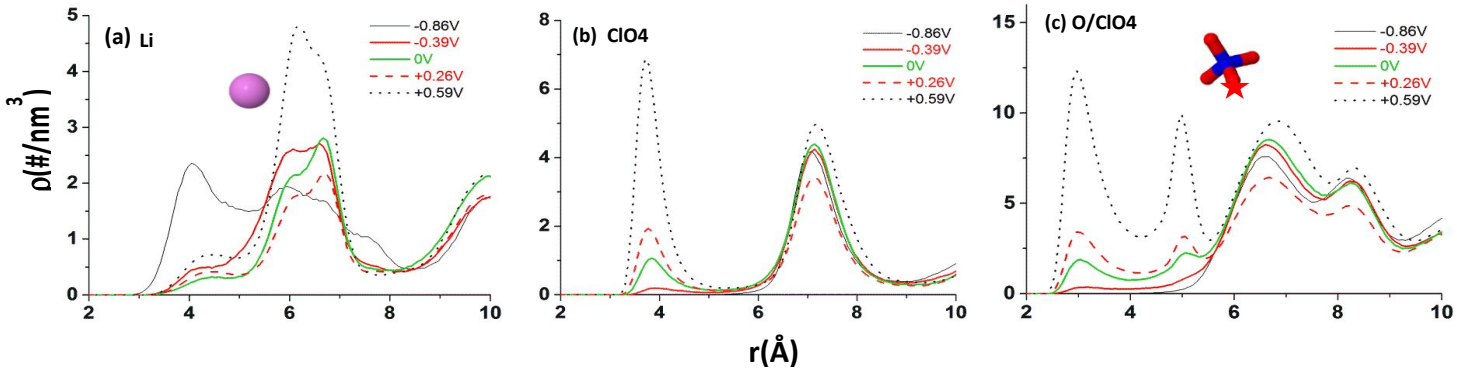

Figure S11 Details of the density profiles of (a) Li (b) center of mass of ClO4 and (c) O atoms of as a function of distance at 5 applied surface potentials. The surface potentials are shown in panel' legends.

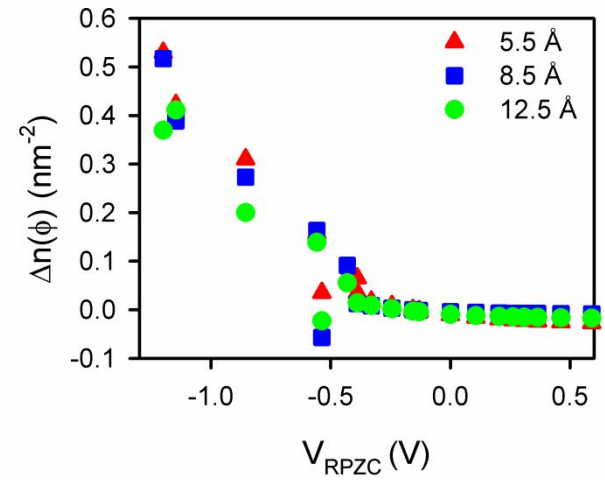

Figure S12. The Li^+ cation interfacial densities from MD simulations relative to V_{RPZC}=0 (data was smoothed for V_{RPZC}>-0.4 V)

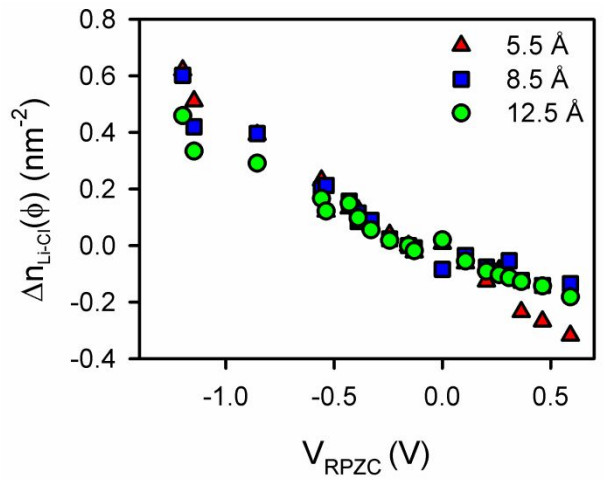

Figure S13. The difference between the Li and Cl(anion) interfacial densities for various interfacial layer widths from MD simulations relative to V_{RPZC}=0.

Note that while traditional theories such as Gouy-Chapman model, consider electrode screening by the solvated solvent separated ions, high degree of $LiClO_4$ ion pairing and aggregation leads to an additional charge screening via charged aggregates such as $[Li_2(ClO_4)]^+$ and $[Li(ClO_4)_2]^-$ and $LiClO_4$ ion pairs forming dipoles.

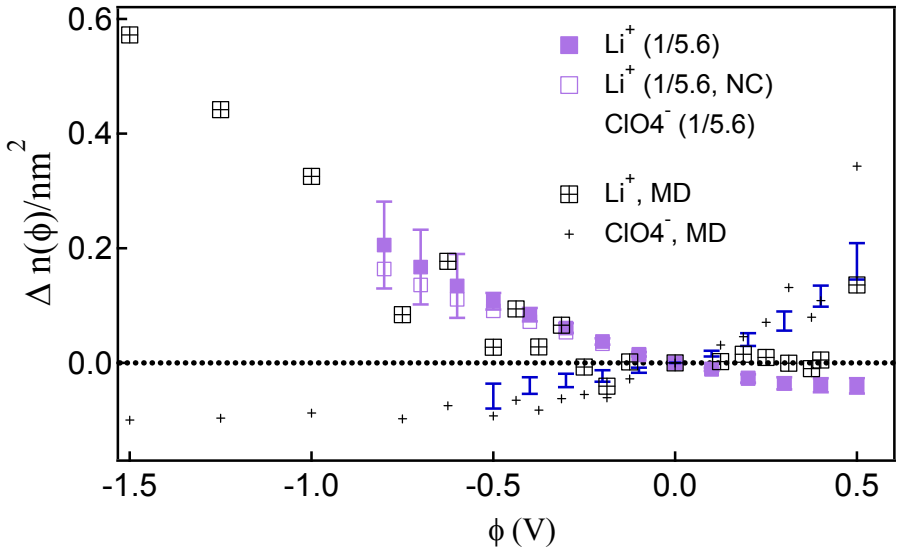

Figure S14 Main manuscript Figure 3 on a potential axes calculated in a different way. The surface potential φ on each individual electrode was dialed such that φ=±ΔU/2 and uncharged (PZC) surfaces have surface voltage φ=0. Shown on an extended scale and with the MD results as points, showing the full scatter.

References

1. Borodin, O.; Smith, G. D., Quantum Chemistry and Molecular Dynamics Simulation Study of Dimethyl Carbonate: Ethylene Carbonate Electrolytes Doped with LiPF6. *J. Phys. Chem. B* **2009,** *113*, 1763-1776.
2. Kameda, Y.; Saito, S.; Umebayashi, Y.; Fujii, K.; Amo, Y.; Usuki, T., Local structure of Li^+ in concentrated $LiPF_6$–dimethyl carbonate solutions. *J. Molec. Liq.* **2015,** *217*, 17-22.
3. Doucey, L.; Revault, M.; Lautié, A.; Chaussé, A.; Messina, R., A study of the Li/Li+ couple in DMC and PC solvents: Part 1: Characterization of LiAsF6/DMC and LiAsF6/PC solutions. *Electrochim Acta* **1999,** *44*, 2371-2377.
4. Marenich, A. V.; Cramer, C. J.; Truhlar, D. G., Universal Solvation Model Based on Solute Electron Density and on a Continuum Model of the Solvent Defined by the Bulk Dielectric Constant and Atomic Surface Tensions. *J. Phys. Chem. B* **2009,** *113*, 6378-6396.